Plasma column stability and beam-driven Trivelpiece–Gould modes in a Gabor lens

Urs Joseph Hecke,[1,2,*] Calvin Dyson,[2,†] and Kenneth Long[2,†]

[1] *Department of Physics, Technical University of Munich, 85748 Garching, Germany*

[2] *Department of Physics, Imperial College London, South Kensington Campus, London SW7 2AZ, UK*

(Dated: August 20, 2026)

The Laser-hybrid Accelerator for Radiobiological Applications (LhARA) proposes Gabor lenses which are cylindrical electron columns confined in a Penning–Malmberg trap to capture and focus laser-accelerated proton beams. The focusing force is provided by the electron density distribution. Simulation of an LhARA-scale lens are done with particle-in-cell code performed with WarpX [1, 2]. The column is initialised as a rigid-rotor thermal equilibrium and stays uniform while the rotation remains rigid. The rotation shears from the centre outward and over one microsecond the core density falls by 9 % while the half-density radius and the axial extent stay stable, so the column hollows without expanding. An 8 MeV proton bunch is then passed through the equilibrated column. The natural density fluctuations are identified as Trivelpiece–Gould modes, fulfilling the cold-column dispersion relation to better than 2 % and the bunch drives an additional mode at the wavenumber where its velocity matches the wave phase velocity. A second shorter bunch with the same density drives that mode more strongly despite carrying less of the charge.

I. INTRODUCTION

Ion beam therapy concentrates dose in a narrow Bragg peak at a depth set by the beam energy, giving better spatial control than conventional radiotherapy [3]. The Laser-hybrid Accelerator for Radiobiological Applications (LhARA) is a proposed facility for studying the radiobiology of such beams [4].

One of the main challenges is the laser-accelerated beamline. After leaving the target the beam has a large radius and is strongly divergent, and it has to be turned into a controlled, high-density focused beam. Conventional quadrupole focusing has the disadvantage of focusing in one transverse plane and defocusing in the other at least two are needed to provide focusing [4]. Gabor lenses, which consist of an electron plasma column through which the proton beam passes, focus in both planes at once. This works with the space charge of the plasma which forces the protons to bent. The beam itself represents a perturbation to the plasma's equilibrium. This paper therefore concentrates on the stability of the column and on the beam's influence upon it, rather than on the beam optics.

Sec. II develops the theory, covering the Gabor lens and its equilibrium, the perturbation caused by the beam, and the principle of PIC simulation. Sec. III explains how the simulations were set up, and Sec. IV analyses the results in the context of that theory.

* urs.hecke@tum.de

† Supervised the project.

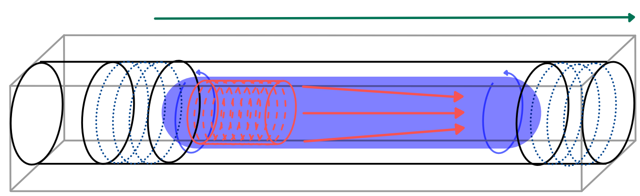

FIG. 1. Schematic design of the Gabor lens: The empty space on the left side is simulation space for inserting the beam, the blue column is the plasma and the two ring areas on both sides of the plasma represent the electrodes and the green arrow shows the direction of the B-field.

II. THEORY

A. Gabor lens

A Gabor Lens, sketched in Fig. 1, follows the principle of a Penning-Malmberg-Trap. End electrodes with a certain voltage in comparison to the wall create a potential well in which the electrons are trapped in the axial direction. The electron distribution is rotating around the axis of symmetry and together with an axis-aligned magnetic field provides radial confinement [5]. For the Gabor lens, the end electrodes get replaced by end rings which allows the proton beam to fire axis-aligned through the plasma. Because of the negative space-charge, the proton beam gets pulled inwardly. In a uniform plasma, this inward force is linear with the radius, providing perfect focusing behaviour [6, pp. 79–81].

B. Equilibrium

Radial equilibrium requires the inward magnetic force to balance three outward contributions: the electric force of the electron cloud's own space charge, the centrifugal force, and the pressure gradient,

$$0 = F_{\mathrm{E}} + F_{\mathrm{B}} + F_{\mathrm{centrifugal}} + F_{\mathrm{pressure}} \tag{1}$$

$$0 = -en(-\frac{\partial \phi}{\partial r} + \omega_r r B) + \frac{mnv_\theta^2}{r} - k_{\mathrm{B}} T \frac{\partial n}{\partial r}. \tag{2}$$

In the cold-fluid approximation where we can drop the pressure term, the equation for the needed angular velocity is

$$\omega_r^{\pm} = \frac{\omega_{ce}}{2}\left(1 \pm \sqrt{1 - \frac{2\omega_{pe}^2}{\omega_{ce}^2}}\right) \tag{3}$$

where $\omega_{ce} = \frac{eB_0}{m_e}$ is the electron cyclotron frequency and $\omega_{pe}^2 = \frac{n_e e^2}{\varepsilon_0 m_e}$ is the electron plasma frequency. A derivation of this relation is given in App. B.
However, as pointed out in Sec. IV, dropping the pressure term is not always justified. In this case, the rigid-rotor angular velocity can be found with a thermal-equilibrium solver (cf. App. D, C).

C. PIC Simulation

When simulating a plasma, every single particle creates its own $\frac{1}{r^2}$-Coulomb field which affects all the other particles except itself. If a plasma consists of 4 particles, $4 \times 3 = 12$ calculations have to be made, for 10 particles 90 calculations, for 100 particles 9900 and for 10^{14} particles one has to do approx 10^{28} calculations for each timestep. This is a classical $O(N^2)$ scaling problem. To solve this, particle-in-cell (PIC) simulations are used amongst others.
PIC introduces so called macroparticles which represent a large number of particles. Those macroparticles carry the cumulative charge of the real particles they represent. Their charge isn't concentrated on a single point but split up on the adjacent grid points. This grid is the second new principle of PIC. It simplifies the simulation space into a discrete number of cells, hence the name *particle-in-cell*.[7, pp. 308–314]
The basic algorithm [8] is:

1. From the current location of the macroparticles, calculate the charge density
2. Solve Poisson's equation to find the potential and electric field
3. Calculate the new location and velocity of macroparticles using Newton's 2nd law
4. Repeat

Simulations were performed using WarpX. The physical and numerical parameters modelling the Gabor lens environment as well as the beam parameters are summarized in Tables I, II and III.

TABLE I. Physical and numerical parameters for the WarpX PIC simulation.

Parameter	Value
Grid dimensions ($X \times Y \times Z$)	$112 \times 112 \times 2048$
Time step (Δt)	8.75 ps
Transverse resolution ($\Delta x = \Delta y$)	$0.775\lambda_{De}$
Longitudinal resolution (Δz)	$0.730\lambda_{De}$
Number of macroparticles	1.54×10^8
Macroparticles per cell (PPC)	12.1

TABLE II. Physical parameters for the WarpX PIC simulation.

Parameter	Value
Lens length	857 mm
Lens radius	36.5 mm
Electrode voltage (axial confinement)	−65 kV
B-field (radial confinement)	0.05 T
On-axis peak density	$5.7 \times 10^{15}\,\mathrm{m^{-3}}$
Flat-top density	$4.8 \times 10^{15}\,\mathrm{m^{-3}}$
Electron temperature (T_e)	75 eV
Rigid rotation $\omega_r/2\pi$ (slow branch)	155.401 MHz
Electron plasma frequency $\omega_{pe}/2\pi$	622.1 MHz
Electron cyclotron frequency $\omega_{ce}/2\pi$	1399.6 MHz
ω_{pe}/ω_{ce}	0.44

D. Plasma perturbation

A proton bunch with $n_b \ll n_e$ perturbs the column weakly. Perturbations can be written as combinations of

$$\delta\phi,\ \delta f \ \propto\ \exp[\,i\,(\ell\theta + k_z z - \omega t)] \tag{4}$$

with ℓ the azimuthal mode number, k_z the axial wavenumber and ω the mode frequency. Single-valuedness in θ restricts ℓ to integers, while k_z is a continuous real parameter because the column is idealised as infinitely long. For given ℓ and k_z the dispersion relation then fixes ω as an eigenvalue. The bunch itself is localised rather than periodic. It can be written as a superposition of such waves. The predicted response separates into a quasi-static rearrangement that travels with

TABLE III. Beam parameters for the WarpX PIC simulation.

Parameter	Bunch A	Bunch B
Common		
Kinetic energy (E_b)	8 MeV	
Velocity v_b	$0.13\,c = 3.89 \times 10^7$ m/s	
Radius	3 cm	
Density (n_b)	$1.8 \times 10^{12}\,\mathrm{m^{-3}}$	
Density distribution	Uniform	
Number of macroparticles	2×10^7	
Per bunch		
Length L_b	19.5 cm	4.74 cm
Duration L_b/v_b	5.0 ns	1.2 ns
Number of protons	1.0×10^9	0.24×10^9

the bunch and screens its charge, and a wave left behind it. Which wave is available is fixed by the geometry. The column is magnetised, $\omega_{pe}/\omega_{ce} = 0.44$, so its dielectric response is anisotropic and the wave frequency depends on the direction of propagation. For a cold, uniform-density non-neutral infinitely long column of radius r_b inside a conducting wall at $r = b$, [9, Eq. (5.69)] gives the exact electrostatic dispersion relation. The complete derivation is in App. E. The perturbation is axisymmetric and injected on axis, so it couples only to $\ell = 0$, leaving

$$\frac{1}{g_0} = -\,\varepsilon_\perp\, T r_b\, \frac{J_1(Tr_b)}{J_0(Tr_b)}, \qquad T^2 = -k_z^2\,\frac{\varepsilon_\parallel}{\varepsilon_\perp}, \tag{5}$$

with $\varepsilon_\parallel = 1 - \omega_{pe}^2/\omega^2$, $\varepsilon_\perp = 1 - \omega_{pe}^2/(\omega^2 - \omega_v^2)$, and g_0 the geometric factor

$$g_l = (k_z r_b)^{-1}\, \frac{K_l(k_z b) I_l(k_z r_b) - K_l(k_z r_b) I_l(k_z b)}{K_l(k_z b) I_l'(k_z r_b) - K_l'(k_z r_b) I_l(k_z b)} \tag{6}$$

where the prime denotes differentiation with respect to the whole argument. $I_l(x)$ and $K_l(x)$ are the modified Bessel functions of first and second kind and

$$\omega_v^2 \equiv (\omega_{re}^+ - \omega_{re}^-)^2 = \omega_{ce}^2 - 2\omega_{pe}^2, \tag{7}$$

following from Eq. (3). A.W. Trivelpiece and R.W. Gould have examined this setup [10] after whom those modes were named: *Trivelpiece–Gould modes.*

III. METHODOLOGY

Prior to simulating the beam travelling through the plasma, the plasma itself has to be in an equilibrium. This can only be achieved approximately. Therefore, the plasma gets initialized in this close-to-equilibrium state. For this a Poisson-Boltzmann solver finds a half-density radius which then gets fed into a thermal-equilibrium solver which returns the distribution. This gets sampled to macroparticles to which the rigid-rotor angular velocity and a random thermal velocity gets added. Nevertheless, the thermal velocity gets added symmetrically in order to not initialize with an azimuthal asymmetry. Lastly, those get fed into WarpX. Because it is just a close-to-equilibrium state, it gets simulated a short period of time, to settle. If the plasma settles to an equilibrium state, this state can afterwards be used for the beam simulation to travel through.

IV. RESULTS

A. Equilibrium

1. Rigid-Rotation

At first, the simulation of both plasma and beam-plasma-interaction was performed in a 28.1 cm long lens (Swansea lens) with a 2.05 cm radius with a target density of $6 \times 10^{13}\,\mathrm{m}^{-3}$ and $T = 2.73\,\mathrm{eV}$. For this simulation, the cold-fluid approach to assign the angular velocity held. However, for the final setup of Tables II and III which corresponds to the LhARA Gabor lens, the simulation exhibited particle loss, radial oscillations and rapid heating. The problem was that a uniform plasma was assumed. By Gauss's law, the radial electric field is $E_r = \frac{\partial \phi}{\partial r} = \frac{enr}{2\varepsilon_0}$. In an volume where the local density is below the uniform density value, the electric field gets underestimated, resulting in an underestimation of the needed magnetic force. That directly corresponds to too low a value of ω_r. The actual plasma self-field was then stronger than anticipated and just pushed the boundary particles out. Because the error scales with r, the plasma became sheared and therefore wasn't in a thermal equilibrium at all. That's why the strong oscillations happened. The problem was solved by using the warm plasma rigid-rotor approach, where the angular velocity gets taken from a thermal-equilibrium solver. It repeatedly solves Poisson's equation and Boltzmann thermal equilibrium condition. The process is described in Appendix C and D. This reduced particle loss from 8.27 % to 4.18 % in the simulated 1 µs.
Another improvement was to reduce the time steps from 50 ps to 8.75 ps, which reduced the loss from 4.18 % to below 1 %. Furthermore, this dropped the heating processes as Table V shows. The resulting equilibrium is summarised in Table IV.

TABLE IV. Mechanical equilibrium.

Quantity	Value
ω_r applied by the sampler	155.4 MHz
Plasma half-density radius, solver input	33.93 mm
Plasma half-density radius, measured	33.89 mm
Particle count over 1 µs	−0.428 %
Canonical angular momentum P_θ over 1 µs	0.295 %

TABLE V. Departure from thermal equilibrium. The heating rate is quoted as the factor by which the mean temperature grows.

Quantity	Δt	Value
Mean T rise per 1 µs	35 ps	×3.55
Mean T rise per 1 µs	17.5 ps	×2.56
Mean T rise per 1 µs	8.75 ps	×2.00
T_z over 2.5 µs	8.75 ps	×1.95
$T_\perp$ over 2.5 µs	8.75 ps	×4.31
Anisotropy $T_\perp/T_z$ at 2.5 µs	8.75 ps	2.28

Generally, the rigid-rotation doesn't hold its initial rigidity. As Figure 2 shows, the plasma rotates rigidly to good approximation for the first third of the simulation. However, beginning from the centre, the plasma loses angular velocity which continues the whole simulation as Figure 2 shows as well. By the end, the centre

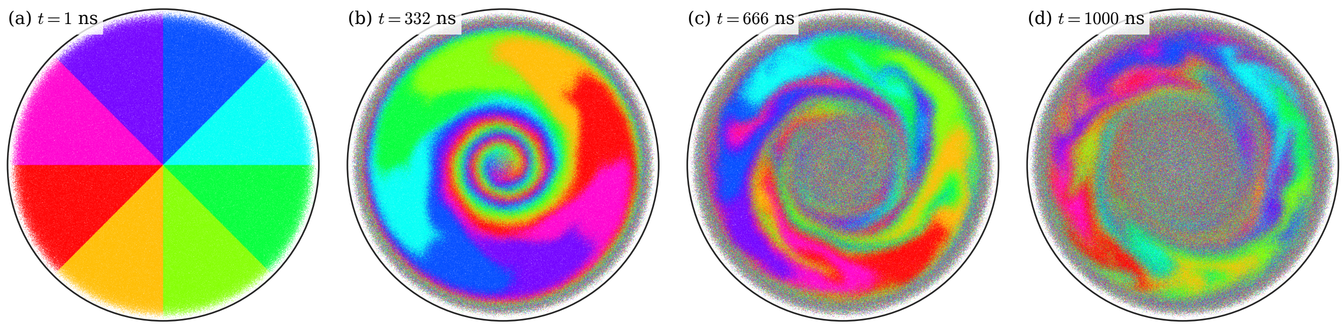

FIG. 2. Differential rotation of the electron column (counterclockwise). Each macroparticle is coloured by the initial azimuthal angle. Only the midplane region $|z| < 0.3\,\mathrm{m}$ is shown, and the outer circle marks the conducting wall at 36.5 mm.

TABLE VI. Radial shear of the rotation rate. Each ring is an annulus of width $0.04\,\mathrm{r/R_p}$ so each is 1.36 mm. The drift is the slope of a least-squares fit to ω measured at 92 times through the 1 µs run, expressed as a percentage of its value at $t = 0$. Uncertainties are standard errors of the fitted slope and assume independent samples

Ring (r/R_p)	Drift (%/µs)
0.18–0.22	-14.9 ± 2.7
0.26–0.30	-12.6 ± 1.7
0.34–0.38	-6.7 ± 1.3
0.42–0.46	-2.8 ± 0.9
0.50–0.54	-1.0 ± 0.7
0.66–0.70	-0.0 ± 0.6
0.90–0.94	$+0.9 \pm 0.4$
0.98–1.02	$+2.9 \pm 0.5$
1.02–1.06	$+5.3 \pm 0.4$

has approximately 15 fewer rotations, resulting in the blurry central area of panels (c) and (d). It is also visible that the middle radii especially the ones between $0.5 - 0.9r/R_p$, crossing zero drift at $0.68r/R_p$, keep their rigidity very good as even after the whole simulation, they remain visibly attached. Table VI also shows that the outer radii even sped up, raising the assumption that angular momentum gets outwardly transferred.

2. Density

The implications following from Sec. IV A 1 show up in the development and stability of the plasma's density. Radially, Fig. 4 (a) and (b) both show that the uniform column starts hollowing from the center. The core density falls from $4.847 \times 10^{15}\,\mathrm{m^{-3}}$ to $4.412 \times 10^{15}\,\mathrm{m^{-3}}$, meaning that the density inside $r = 5\,\mathrm{mm}$ changes by $-9\,\%$. On the other hand, the plasma half-density radius R_p stays quite stable with 33.88 mm to 34.01 mm. Connecting both means that the plasma hollows from the centre but not with the result of an expanding radius. Both effects are visible in Fig. 4 (a). Axially, the plasma is basically stable, changing its half-extent by $< 0.05\,\%$.

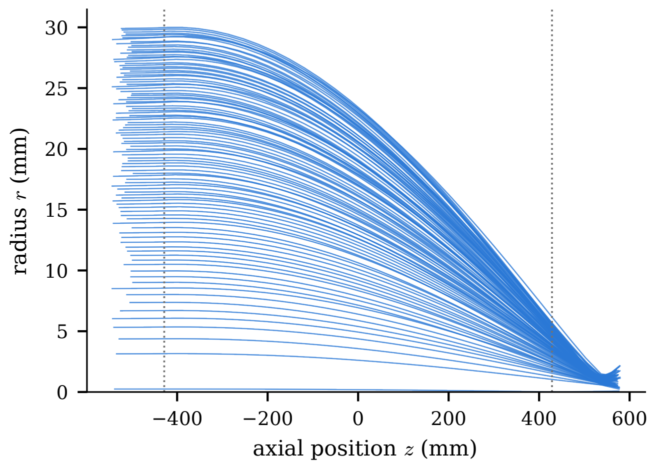

FIG. 3. Trajectories of 8 MeV protons passing through the electron column. One hundred of the 2×10^7 beam macroparticles are shown. The dotted lines mark the gate electrodes at $z = \pm 428.5\,\mathrm{mm}$.

Connecting this to the results from Sec. IV A 1, the electrons start redistributing in the column without expanding it. Nevertheless, Fig. 3 shows that in the scope of this research, the focusing effect isn't badly disrupted by this. The beam enters with a 30 mm radius and passes the second electrode with a 8 mm radius.

B. Interaction

1. Resonance condition

The bunch crosses the plasma at fixed velocity. It can be seen as a superposition of perturbation of the form of Eq. (4) which have the phase velocity v_b. Therefore, their dispersion relation is $\omega = k_z v_b$. Among all of TG waves the plasma supports one has phase velocity equal to v_b. Plotting ω against k_z gives a straight line with slope v_b. Where that line crosses the TG dispersion curve is the one (k_z, f) satisfying both $\omega = k_z \cdot v_b$ and the dispersion

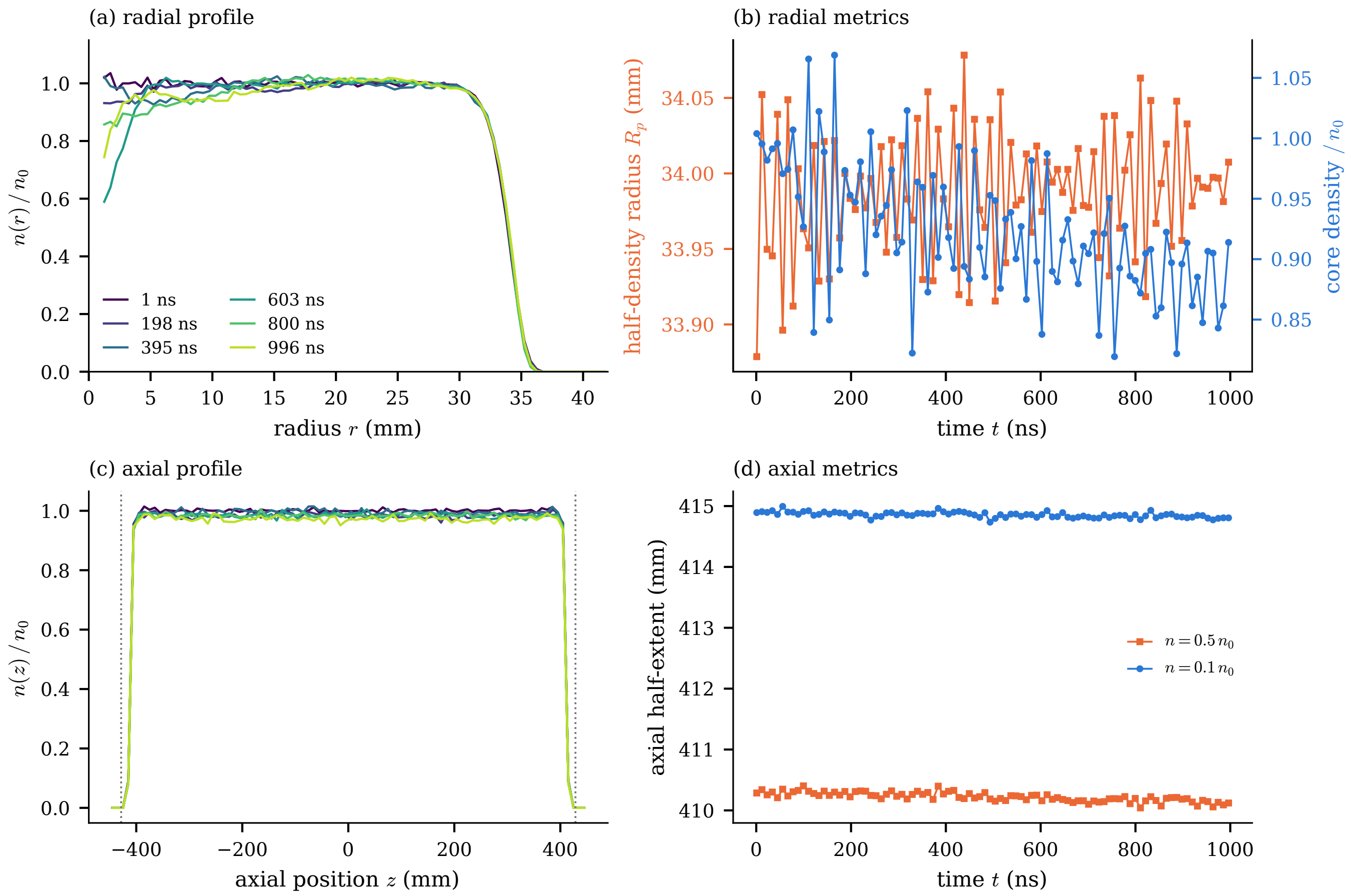

FIG. 4. Stability of the electron column over the 1 µs equilibration run, sampled at 92 times. All panels use a single fixed reference, $n_0 = 4.828 \times 10^{15}/\mathrm{m}^3$, the area-weighted mean density inside $r = 25\,\mathrm{mm}$ at $t = 0$. (a) Radial density profile, measured in the midplane slab $|z| < 0.3\,\mathrm{m}$. (b) Half-density radius R_p (left axis) and core density, the area-weighted mean inside $r = 5\,\mathrm{mm}$ (right axis). (c) Axial density profile for particles within $r < 20\,\mathrm{mm}$. The dotted lines mark the gate electrodes at $z = \pm 428.5\,\mathrm{mm}$. (d) Axial half-extent.

relation simultaneously. This is the mode the beam can resonate.

2. Spectral analysis

The simulation was carried out twice. It was the exact same setup, except bunch A was 19.5 cm long and bunch B was 4.74 cm long, while keeping the proton density constant. For both runs, a control and an interaction run were done to see which plasma behaviours are beam induced and which are normal fluctuation. The important parameters for both bunches are given in Table III.

The electron distribution is binned into 256 axial cells over $|z| < 0.4175\,\mathrm{m}$ keeping particles within $r < 3\,\mathrm{cm}$ and therefore excluding the boundary effects in the following analysis. Frames are recorded every 0.875 ns. The interaction analysis uses $0 < t < 22\,\mathrm{ns}$ because 22 ns is the beam's transit time. Therefore, the finite length can't have any effect here. Each cell's time series gets normalised to its own mean and the per-frame mean subtracted. Then, a 2D FFT in (z, t) is applied, giving $P(k_z, f)$, whose exact definition is given in Appendix F, but basically is the fluctuation density on a (k_z, f)-map. The resulting resolutions are listed in Table VII.

TABLE VII. Spectral analysis parameters.

Quantity	Bunch A	Bunch B
Common		
Frame interval Δt	0.875 ns	
$\Delta k_z = 2\pi/L$	7.52/m	
$k_{z,\mathrm{max}} = \pi/\Delta z$	963/m	
$f_{\mathrm{Nyq}} = 1/2\Delta t$	571.4 MHz	
Dispersion (Fig. 5)		
Frames	58	115
Record length	50.8 ns	100.6 ns
$\Delta f = 1/T_{\mathrm{rec}}$	19.70 MHz	9.94 MHz
Interaction (Fig. 7)		
Frames	25	25
Record length	21.9 ns	21.9 ns
$\Delta f = 1/T_{\mathrm{rec}}$	45.7 MHz	45.7 MHz

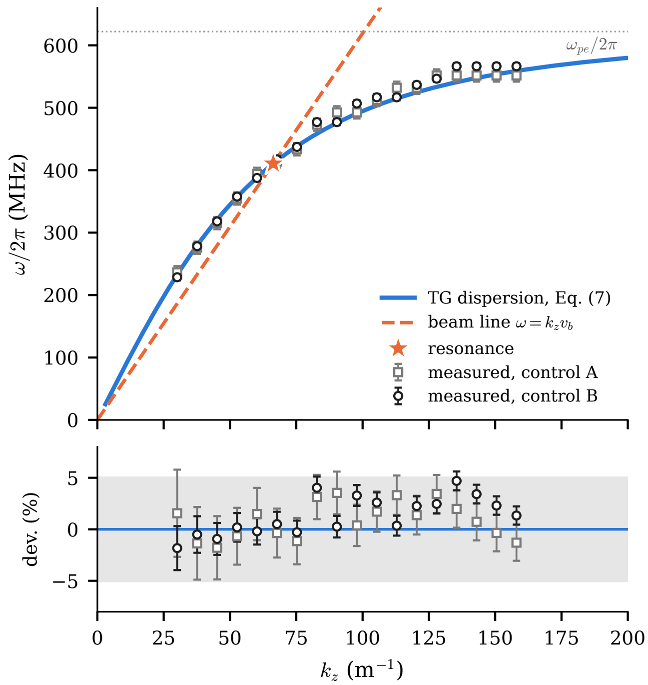

FIG. 5. Trivelpiece–Gould dispersion relation. Upper panel: the solution of the dispersion relation (5) and the beam line. The two intersect at $k_z = 66.31$/m and $\omega/2\pi = 410.5$ MHz (star), which is the wavenumber at which the bunch and the plasma mode share a phase velocity. Points are from the V-shaped area of the density fluctuation spectrum measured from the control runs. The criterion is the highest peak-to-median contrast. Error bars of half a frequency bin. Lower panel: deviation of the measured frequencies from the prediction. Above $k_z \approx 80$/m the branch frequency approaches the Nyquist limit set by the diagnostic cadence and the measured points drift systematically high.

3. *Dispersion of the unperturbed column*

As Figure 5 shows, the strongest detected fluctuations from the control runs sit closly or on the dispersion relation. Over the 18 tracked wavenumbers, the measured frequencies deviate on average by 1.65 % for A and 1.75 % for B from the TG dispersion relation. Two independent runs of different length therefore reproduce the same branch, and the natural fluctuations of the column are already TG modes. The intersection between the theory solution (5) and the beam line gives the theoretically driven TG mode, noted down in Table VIII.

TABLE VIII. Predicted TG mode

Parameter	Value
Wavelength (λ_z)	9.475 cm
Frequency $\omega/2\pi$	410.54 MHz
Wavenumber k_z	66.310/m

4. *Beam-driven response*

The left plots in Figure 6 show $P(k_z, f)$ from the control runs. The solution of the dispersion relation is overlaid and follows the V-shaped area, stating again that the fluctuations are TG modes. The symmetry in the plot is a confirmation that the fluctuations in our plasma propagate equivalently in both directions, confirming correct behaviour.

The right-hand panels of Figure 6 show the driven power $P_{\text{beam}} - P_{\text{control}}$. Since the bunch drives every wavenumber at $\omega = k_z v_b$, the driven power is read along that line, and the same quantity at $-k_z$, which the bunch cannot drive, provides the noise floor.

Figure 7 shows this cut through both maps. For bunch B the driven power rises from the noise floor at $k_z \approx 38$/m, peaks at $k_z = 67.7$/m, the predicted crossing of Table VIII. Bunch A shows the same feature, with its maximum one bin above the crossing. For both bunches the counter-propagating side is flat at every wavenumber as expected. The values are collected in Table IX.

Below $k_z = 30$/m a second, unrelated response appears, spanning 46 MHz to 183 MHz at $k_z = 15$/m to 23/m, which gets excluded from the analysis because these wavenumbers correspond to $\lambda_z = 28$ cm to 42 cm, meaning that this is some kind of global plasma oscillation. The interaction analysis is therefore restricted to $k_z \geq 30$/m.

TABLE IX. Driven power at the predicted crossing. The counter-propagating scatter is the noise floor, since the bunch cannot drive modes with $k_z < 0$.

Quantity	Bunch A	Bunch B
$P_{\text{beam}} - P_{\text{control}}$ at $k_z = 67.7$/m	0.0993	0.1894
Maximum along the beam line	0.1048	0.1894
at k_z (1/m)	75.25	67.72
Counter-propagating scatter	0.0026	0.0020
Ratio B/A at the crossing		1.91

Table IX shows that the shorter bunch drives the mode more strongly. This is connected to the bunch length, since the proton number was reduced for the 4.74 cm bunch to leave the density unchanged. This makes bunch B, although the smaller perturbation in charge, the stronger driver. To understand this behaviour, the form-factors have to be taken into account.

The predicted wave length of the TG mode $\lambda = 9.475$ cm fits approximately twice in bunch A's length of 19.5 cm and is double the length of bunch B which is 4.74 cm. A bunch of length 9.475 cm can be viewed as two attached pieces, each half a wave length. The first half would drive a TG mode, the second would drive the same TG mode but shifted by exactly half a wave length backwards, resulting in destructive interference of both. This argument can be repeated for a bunch of two wavelengths. It would also be the reason why a bunch of half a wavelength doesn't cancel out. However, since A is still quite

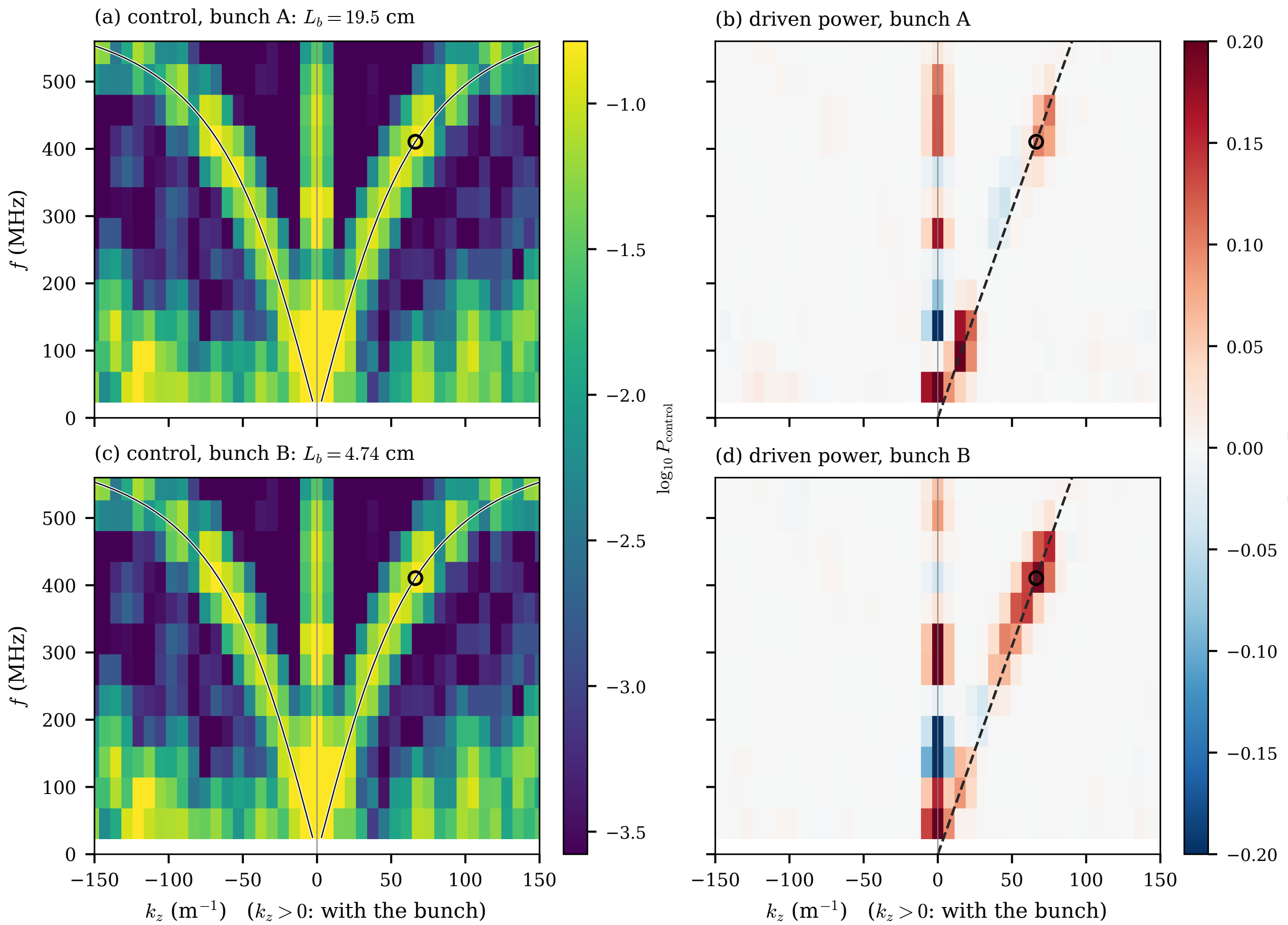

FIG. 6. Density fluctuation spectra in the (k_z, f) plane. All plots have the predicted resonance circled. Left: the beam-free control for each bunch, with the solution of the dispersion relation Eq. (5) overlaid. The analysis is restricted to $k_z \geq 30$/m. Right: $P_{\text{beam}} - P_{\text{control}}$ for each bunch on a common colour scale, with the beam line dashed.

present even though it should be close to completely] gone, according to this destructive interference theory, there might be another factor not covered in this analysis.

V. DISCUSSION AND CONCLUSION

Three results follow from the analysis. First, the rigid-rotor equilibrium holds only for as long as the rotation stays rigid: the column rotates uniformly through roughly the first third of the run. Then the centre density begins to hollow and angular momentum is transported outwards. Over one microsecond the core density falls by 9 % while the the half-density radius and the axial stay relatively stable, so the electrons redistribute inside the column rather than escaping it. Second, the natural density fluctuations of the unperturbed column are Trivelpiece–Gould modes: their measured dispersion follows the cold-column relation of Eq. (5) to better than 2 % across eighteen wavenumbers and two independent runs reproduce the same branch. Third, a passing proton bunch drives a mode at the wavenumber where its velocity matches the wave phase velocity. A 4.74 cm proton bunch drives it approximately twice as strong as a 19.5 cm one does.

From this, two implications follow for the Gabor lens: A beam travelling through the column will resonantly excite a Trivelpiece–Gould mode whenever its velocity coincides with a mode's phase velocity. However, the perturbation measured here is weak: Neither the density profile or the proton trajectories are visibly disturbed by the passage of a single bunch, and the beam is still focused.

Important limitations weaken these conclusions. The equilibration was followed for 1 µs, which is short compared to a realistic usage, and the heating had not saturated by the end of the run, meaning that no prediction about its further influence can be made. The interaction runs begin from the state reached after the 1 µs run, which didn't reach a real equilibrium. Finally, the form-factor argument needs to be derived mathematically for

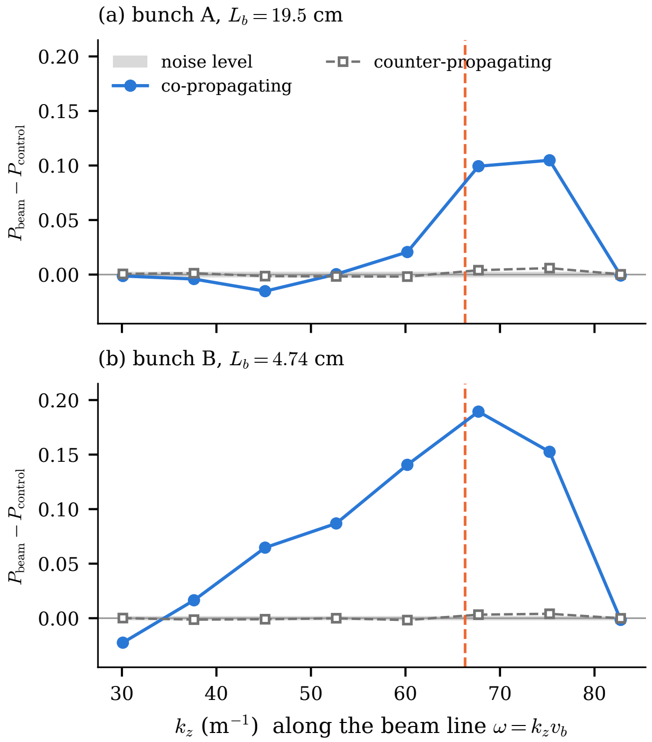

FIG. 7. Driven power $P_{\mathrm{beam}} - P_{\mathrm{control}}$ along the beam line $\omega = k_z v_b$, measured over the transit window $0 < t < 22$ ns. Filled circles: co-propagating. Open squares: counter-propagating, giving the noise floor (grey band). The dashed line marks the predicted crossing. (a) Bunch A, 19.5 cm. (b) Bunch B, 4.74 cm, whose maximum coincides with the predicted crossing.

a full understanding. In the future, longer equilibration runs to test the heating and hollowing would need to be done to check whether it saturates. Repeated beam-driven runs have to be done to check appearance of the driven mode because it was only measured in this specific equilibrium setup. The dispersion relation for a finite long column needs to be derived and checked to make statements about longer time scales. Lastly, an actual experiment to test all results would be needed to verify all the stated results from simulations.

Appendix A: Numerical Validation

PIC simulation must fulfil several conditions to work properly [11]:

- The spatial grid has to resolve the electron Debye-length.
- The integration timestep of the equations of motion has to be small enough to ensure that trajectories are computed accurately.
- The collision probabilities in each timestep should be sufficiently small.
- Particles should not fly a longer distance during a timestep than the grid division, as expressed by the Courant–Friedrichs–Lewy (CFL) condition.
- Accurate results require a high number of particles per gridcell.

All of these were checked for the simulations done as Tab. I shows.

Appendix B: Derivation of the angular velocity in the cold-fluid approximation

We begin with the general multi-species fluid equilibrium rotation equation for species j which valid if

- the plasma is uniform in z-direction,
- the equilibrium radial density and velocity profiles are azimuthally symmetric and
- the plasma components are assumed to be sufficiently cold that dropping the pressure term in the force balance is a good approximation.

$$\omega_{rj}^{\pm} = -\frac{\mathrm{sgn}(q_j)\omega_{cj}}{2}\left(1 \pm \sqrt{1 - \sum_k \frac{2e_j \hat{n}_k e_k}{\varepsilon_0 m_j \omega_{cj}^2}}\right). \tag{B1}$$

For a single-species electron plasma ($j = e$, $e_e = -e$), the sum collapses to $k = e$, yielding:

$$\omega_r^{\pm} = \frac{\omega_{ce}}{2}\left(1 \pm \sqrt{1 - \frac{2n_e e^2}{\varepsilon_0 m_e \omega_{ce}^2}}\right). \tag{B2}$$

Substituting the electron plasma frequency $\omega_{pe}^2 = \frac{n_e e^2}{\varepsilon_0 m_e}$ recovers:

$$\omega_r^{\pm} = \frac{\omega_{ce}}{2}\left(1 \pm \sqrt{1 - \frac{2\omega_{pe}^2}{\omega_{ce}^2}}\right). \tag{B3}$$

Appendix C: Derivation of the angular velocity without the cold-fluid approximation

As shown in [9, pp.52–54], particle distributions of the form $f(r,\vec{p}) = F(H - \omega_{re}P_\theta)$ have $V_\theta(r) = \omega_{re} r$ as the mean azimuthal velocity of an electron fluid element. This is a rigid rotation around the axis of symmetry with ω_{re}. In thermal equilibrium, the rigid-rotor distribution function is

$$f(r,\vec{p}) = \frac{\hat{n}_e}{(2\pi m_e k_B T_e)^{\frac{3}{2}}} \exp\left[-\frac{H - \omega_{re}P_\theta}{k_B T_e}\right] \tag{C1}$$

with the conserved total energy $H = \frac{1}{2m_e}(p_r^2 + p_\theta^2 + p_z^2) - e\phi_0(r)$ and conserved angular momentum $P_\theta = r(p_\theta - \frac{m_e r \omega_{ce}}{2})$.

The argument of the exponential becomes

$$\begin{aligned} H - \omega_{re}P_\theta = &\frac{1}{2m_e}\left(p_r^2 + (p_\theta - m_e\omega_{re} r)^2 + p_z^2\right) \\ &+ \frac{m_e}{2}\underbrace{\omega_{re}(\omega_{ce} - \omega_{re})}_{K} r^2 - e\phi_0(r), \end{aligned} \tag{C2}$$

i.e. a shifted Maxwellian in the momenta plus the effective potential

$$\psi(r) = \frac{m_e}{2} K r^2 - e\phi_0(r). \tag{C3}$$

The momentum integral is Gaussian in $p_\theta - m_e\omega_{re} r$ and cancels the normalisation, leaving

$$n_e(r) = \hat{n}_e \exp\left[-\frac{\psi(r)}{k_B T_e}\right]. \tag{C4}$$

Equation (C4) is the rigid-rotor Boltzmann relation that closes the Poisson system in App. D. Inverted, it also recovers the rotation frequency from a converged equilibrium. Evaluating (C4) and (C3) on the midplane $z = 0$ gives

$$K = \frac{2}{m_e r^2}\left[k_B T_e \ln\frac{n_e(0,0)}{n_e(r,0)} + e\big(\phi_0(r,0) - \phi_0(0,0)\big)\right]. \tag{C5}$$

Inverting the definition $K = \omega_{re}(\omega_{ce} - \omega_{re})$ then gives

$$\omega_{re} = \frac{\omega_{ce}}{2}\left(1 \mp \sqrt{1 - \frac{4K}{\omega_{ce}^2}}\right), \tag{C6}$$

the slow ($-$) and fast ($+$) rotation branches.

Appendix D: The thermal-equilibrium solver

The initial electron distribution is generated by a self-consistent Poisson–Boltzmann solver following Spencer, Rasband and Vanfleet [12], which returns the equilibrium density $n_e(r,z)$ and potential $\phi_0(r,z)$ of a rigid-rotor thermal equilibrium in the trap geometry.

The solver closes the rigid-rotor density (C4) against Poisson's equation,

$$\nabla^2\phi_0 = \frac{e\,n_e}{\varepsilon_0}. \tag{D1}$$

The system is nonlinear and is solved by iterating between the two with under-relaxation until the density stops changing. Dirichlet conditions at the wall and the axial ends are the only place the electrode geometry enters.

Its one free parameter is the plasma size, imposed through the half-density radius R_p. Setting $n_e(R_p,0) = \frac{1}{2}n_e(0,0)$ in (C5) fixes

$$K = \frac{2}{m_e R_p^2}\Big[\,k_B T_e \ln 2 + e\big(\phi_0(R_p,0) - \phi_0(0,0)\big)\Big], \tag{D2}$$

re-evaluated at every iteration as ϕ_0 converges.

Appendix E: Derivation of Dispersion Relation

For a cold, uniform-density, non-neutral, infinitely long column of radius r_b inside a conducting wall at $r = b$, Ref. [9, pp. 242–247] gives the exact electrostatic dispersion relation.

$$\frac{1}{g_\ell} - \left[1 - \sum_j \frac{\omega_{pj}^2}{D_j}\right] Tr_b\,\frac{J_\ell'(Tr_b)}{J_\ell(Tr_b)} = \ell \sum_j \frac{\varepsilon_j\omega_{cj} + 2\omega_{rj}}{\Omega_j}\,\frac{\omega_{pj}^2}{D_j}. \tag{E1}$$

where $\Omega_j = \omega - k_z V_j - \ell\omega_{rj}$, $D_j = \Omega_j^2 - (\omega_{rj}^+ - \omega_{rj}^-)^2$ and T defined via

$$T^2 \equiv -k_z^2\left[1 - \sum_j \frac{\omega_{pj}^2}{\Omega_j^2}\right] \times \left[1 - \sum_j \frac{\omega_{pj}^2}{D_j}\right]^{-1}. \tag{E2}$$

Since the plasma's only species is electrons, the sum over j reduces to a single term ($j = e$).

$$\frac{1}{g_\ell} - \left[1 - \frac{\omega_{pe}^2}{D_e}\right] Tr_b\,\frac{J_\ell'(Tr_b)}{J_\ell(Tr_b)} = \ell\,\frac{(\varepsilon_e\omega_{ce} + 2\omega_{re})}{\Omega_e}\,\frac{\omega_{pe}^2}{D_e}, \tag{E3}$$

with T correspondingly reducing to

$$T^2 = -k_z^2\left[1 - \frac{\omega_{pe}^2}{\Omega_e^2}\right] \times \left[1 - \frac{\omega_{pe}^2}{D_e}\right]^{-1}. \tag{E4}$$

The equilibrium has no axial drift, $V_e = 0$, and the beam perturbation is axisymmetric, coupling only to $\ell = 0$. Setting $\ell = 0$ leaves $\Omega_e \equiv \omega - k_z V_e - \ell\omega_{re} \to \omega$ and therefore $D_e = \Omega_e^2 - (\omega_{re}^+ - \omega_{re}^-)^2 \to \omega^2 - (\omega_{re}^+ - \omega_{re}^-)^2$ and annihilates the entire right-hand side of Eq. (E3)

$$\frac{1}{g_0} - \left[1 - \frac{\omega_{pe}^2}{\omega^2 - (\omega_{re}^+ - \omega_{re}^-)^2}\right] Tr_b\,\frac{J_0'(Tr_b)}{J_0(Tr_b)} = 0. \tag{E5}$$

From Eq.(3) follows $(\omega_{re}^+ - \omega_{re}^-)^2 = \omega_{ce}^2 - 2\omega_{pe}^2 \equiv \omega_v^2$, recovering the quantity defined in Eq. (7). The same substitution in Eq. (E4), together with $\Omega \to \omega$, gives

$$T^2 = -k_z^2\,\frac{1 - \omega_{pe}^2/\omega^2}{1 - \omega_{pe}^2/(\omega^2 - \omega_v^2)} = -k_z^2\,\frac{\varepsilon_\parallel}{\varepsilon_\perp}, \tag{E6}$$

identifying the two bracketed factors as $\varepsilon_\parallel$ and $\varepsilon_\perp$. This is Eq. (5)'s definition of T^2 in the main text. With $J_0'(x) = -J_1(x)$ and Eq. (E5), one gets

$$\frac{1}{g_0} = -\varepsilon_\perp\,Tr_b\,\frac{J_1(Tr_b)}{J_0(Tr_b)}, \tag{E7}$$

which is Eq. (5).

Appendix F: Definition of $P(k_z, f)$

n_{jl} stands for the electron count in axial cell l at frame j, the relative fluctuation used in the transform is

$$\delta_{jl} = \frac{n_{jl}}{\langle n_{jl}\rangle_j} - 1 - \left\langle \frac{n_{jl}}{\langle n_{jl}\rangle_j} - 1 \right\rangle_l, \tag{F1}$$

where $\langle\cdot\rangle_j$ is an average over frames and $\langle\cdot\rangle_l$ an average over cells. The first term normalises each cell to its own time average, removing the static axial profile, and the second removes the spatial mean of each frame, which carries the $k_z = 0$ component associated with global particle loss and breathing of the column. The spectrum is the squared modulus of the windowed two-dimensional transform [13],

$$P(k_z, f) = \left|\sum_j \sum_l w_j^t\,w_l^z\,\delta_{jl}\,e^{-i(k_z z_l + 2\pi f t_j)}\right|^2, \tag{F2}$$

with w^t and w^z Hann windows in time and in z. Since δ_{jl} is dimensionless, P carries only the arbitrary normalisation of the transform and the window, and every quantity reported is the difference of two spectra computed identically.

ACKNOWLEDGMENTS

This work was conducted as part of the International Research Opportunities Programme (IROP) at Imperial College London.

I would like to express my sincere gratitude to Calvin Dyson and Kenneth Long for their supervision, insightful discussions, and continuous support throughout this project. Further thanks go to Poram Ruksasakchai and Aled Isaac from the University of Swansea.

I acknowledge computing resources provided by Imperial College London and support from the LhARA collaboration.

The analysis scripts and figures presented here were partly produced with the assistance of Claude Code. All results were checked by the author, who takes full responsibility for the content of this paper.

[1] J.-L. Vay, A. Almgren, J. Bell, L. Ge, D. P. Grote, M. Hogan, O. Kononenko, R. Lehe, A. Myers, C. Ng, J. Park, R. Ryne, O. Shapoval, M. Thévenet, and W. Zhang, Nuclear Instruments and Methods in Physics Research A **909**, 476 (2018).

[2] L. Fedeli, A. Huebl, F. Boillod-Cerneux, T. Clark, K. Gott, C. Hillairet, S. Jaure, A. Leblanc, R. Lehe, A. Myers, C. Piechurski, M. Sato, N. Zaim, W. Zhang, J.-L. Vay, and H. Vincenti, in *SC22: International Conference for High Performance Computing, Networking, Storage and Analysis* (2022) pp. 1–12.

[3] H. Paganetti, ed., *Proton Therapy Physics*, 3rd ed., Series in Medical Physics and Biomedical Engineering (CRC Press, Boca Raton, FL, 2025).

[4] The LhARA Collaboration, *ITRF/LhARA Conceptual Design Report*, Tech. Rep. (UKRI Science and Technology Facilities Council (STFC), Swindon, UK, 2026).

[5] D. Gabor, Nature **160**, 89 (1947).

[6] T.-S. Dascalu, *Study of non-neutral electron plasma lenses for focusing laser-driven ion beams*, Ph.D. thesis, Imperial College London (2020).

[7] C. K. Birdsall and A. B. Langdon, *Plasma Physics Via Computer Simulations* (Taylor & Francis Group, 2005).

[8] L. Brieda, The Electrostatic Particle In Cell (ES-PIC) Method, `https://www.particleincell.com/2010/es-pic-method/` (2010), accessed: Jul. 20, 2026.

[9] R. C. Davidson, *Physics Of Nonneutral Plasmas* (Imperial College Press and World Scientific Publishing Co. Pte. Ltd., 2001).

[10] A. W. Trivelpiece and R. W. Gould, Journal of Applied Physics **30**, 1784 (1959).

[11] M. Vass, P. Palla, and P. Hartmann, Plasma Sources Science and Technology **31**, 064001 (2022).

[12] R. L. Spencer, S. N. Rasband, and R. R. Vanfleet, Physics of Fluids B: Plasma Physics **5**, 4267 (1993).

[13] D. B. Percival and A. T. Walden, *Spectral Analysis for Physical Applications* (Cambridge University Press, 1993).